Simulations of the generation and transport of a 5 MV end-point x-ray beam on a pulsed power generator

A. S. Richardson, J. C. Zier, J. T. Engelbrecht, S. B. Swanekamp, and J. W. Schumer
Plasma Physics Division, Naval Research Laboratory, Washington, DC 20375, USA

D. Mosher and P. F. Ottinger
Independent consultant through Syntek Technologies Inc, Fairfax, Virginia 22031, USA

D. L. Duke, T. J. Haines, M. P. McCumber, and A. Gehring
Los Alamos National Laboratory, Los Alamos, New Mexico 87545, USA

(Received 8 February 2019; published 13 May 2019)

An experimental campaign was recently completed at the U.S. Naval Research Laboratory's Mercury pulsed-power facility, where the feasibility of using a 5 MV inductive voltage adder (IVA) as a pulsed photoneutron source was studied. In these experiments, a large-area bremsstrahlung diode was fielded on the Mercury accelerator, producing an intense, pulsed x-ray beam, which generated photoneutrons when striking an appropriate target. This paper reports on simulations that were performed to study the production of the electron beam in the diode, and the generation and transport of the x-ray beam. Comparison is made between the numerically predicted beam properties and results obtained during the experimental campaign. Various models of electron and ion emission from the electrodes in the generator were simulated, and the effect of model parameter choices on the dose predictions is described.

DOI: 10.1103/PhysRevAccelBeams.22.050401

I. BACKGROUND AND INTRODUCTION

Production of an intense pulse of photoneutrons was demonstrated at the U.S. Naval Research Laboratory's Mercury pulsed-power facility [1] in an experimental campaign conducted in 2017. In this campaign, a large-area bremsstrahlung diode was fielded on the Mercury accelerator, which is an inductive voltage adder (IVA) that was configured to produce a high-current electron pulse where the main pulse is approximately 50 ns long with peak voltage near 5 MV. When this electron pulse hits the anode, an intense, pulsed x-ray beam is generated via bremsstrahlung emission produced in a layer of high-atomic-number material. During this campaign, an appropriate target was fielded in this x-ray beam, and the pulse of photoneutrons produced in this target was measured. This method of producing a pulse of x-rays and neutrons has various applications, such as detection of special nuclear material [2].

In conjunction with these experiments, a modeling effort was carried out in which the x-ray production and transport for these experiments was simulated. This paper describes the process that was used to simulate the production of the electron beam, and the subsequent x-ray production and transport. (Neutron production calculations were also performed, but will be reported elsewhere.) The simulated x-ray doses are found to closely match the measured doses, giving confidence in the predictive capabilities of these simulations when applied to an inductive voltage adder (IVA) such as Mercury running at 5 MV. A test suite of additional simulations were performed in order to examine the sensitivity of the simulation results to various electron and ion emission model parameters that are present in the code. Quantifying the uncertainties in the simulation in this way can increase our confidence in the simulation results, and can also improve our understanding of the physical systems being modeled.

The large-area bremsstrahlung diode used in these experiments is, in several ways, a prime candidate for the type of simulation sensitivity study reported here. First, this diode produces a current density on the anode on the order of 100 A/cm^2. At these current densities, the energy deposited into the anode by the electron beam is low enough that the anode survives each shot. This allows the same diode hardware to be used for a large number of shots, giving an extensive dataset for comparison with experiments. Another property that makes this diode a good case for a simulation sensitivity study is the large spacing (~10 cm radially and ~20 cm axially) between the anode

and cathode surfaces. Because of these large gaps, the plasmas that form on the surfaces do not have time to expand significantly into the gap before the pulse is over, which limits the effect that surface plasmas have on the diode impedance. This is helpful from a simulation standpoint, because impedance collapse caused by surface plasmas is notoriously hard to simulate in high-power diodes with small gap spacings (although some progress is being made [3–8]).

One final aspect of this system that makes it a good candidate for a simulation sensitivity study is the nature of the surface emission models used to simulate this diode. Specifically, there are several electron and ion emission models that are needed to capture the physics that is important in this diode. The physical approximations underlying these models are fairly well understood, and result in models that contain parameters which can affect the simulation results [9,10]. The values for some of these parameters are not well known. Additionally, while it is known qualitatively how changing some of these parameters will change the simulation results, the sensitivity of the results to changes in the parameter values for diode systems such as this one is not known quantitatively. Understanding this sensitivity can give a better idea of how much confidence can be placed on the simulation results. (Details of the models and their parameters will be described in Sec. VI.)

In this work, we have not tried to tune the model parameters until the simulation matches the experimental results as closely as possible. Rather, we have systematically examined the model parameters in order to understand their effects and the sensitivity of the results to changes in their values.

Simulation of the x-ray production and transport was performed in a two-step process. The first step in the simulation process was to perform particle-in-cell (PIC) simulations of the Mercury magnetically-insulated transmission line (MITL) and the large-area bremsstrahlung diode. The result of these simulations is the complete, time-integrated, particle distribution of the electron beam produced by the Mercury accelerator. These electrons were then used as source particles for the second step: a Monte Carlo (MC) simulation of the tantalum bremsstrahlung converter, x-ray transport (through the air in the room), and dose deposition in CaF_2 thermoluminescent dosimeters (TLDs). The MC simulation provided time-integrated information about the x-ray beam used to calculate the dose at the locations of the faceplate and far-field TLD arrays for comparison with measured dose data. The diagram in Fig. 1 shows schematically the relationship between the PIC and MC simulation regions and the experimental geometry. An additional step in the simulation process was a MC simulation of the neutron production in various photoneutron targets, but this is beyond the scope of this paper, and will be reported elsewhere.

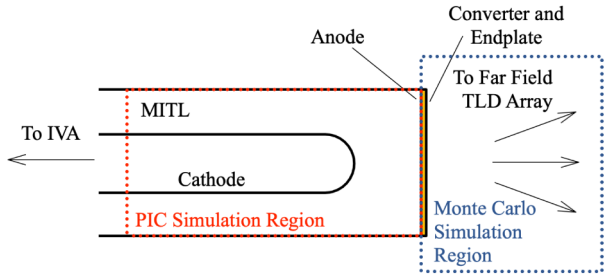

FIG. 1. Diagram showing the locations of the PIC and MC simulation regions, in relation to the geometry of the experiment.

Comparing the simulated and experimentally measured dose distributions provides an important step in ensuring that the simulation process is rigorously tested. These comparisons provide a benchmark for the model of the pulsed power transmission line, the bremsstrahlung diode, and the resulting x-ray beam. Close agreement between the simulated and measured doses shows that the same modeling, performed within the same parameter regime as the Mercury tests, can serve as an accurate method for designing improved source and detection diagnostics for future pulsed neutron sources.

This paper is arranged as follows. In Sec. II, the measurements of the current pulse produced by the Mercury accelerator are described. In Sec. III, the particle-in-cell simulations of the generator and x-ray diode are described, and comparison is made between the simulated and measured current pulses. Section IV describes the TLD dose measurements, and Sec. V describes the Monte Carlo simulations of the dose produced by the simulated x-ray beam. Section VI describes the emission model variations that were simulated, and compares the results of these simulations to the experimentally measured doses. Conclusions are in Sec. VII. Appendix details how the voltage drive for the PIC simulations was generated from the measured currents.

II. ELECTRICAL DIAGNOSTICS OF THE MERCURY GENERATOR

The Mercury pulsed-power accelerator is a six-cell inductive voltage adder (IVA) which drives a magnetically-insulated transmission line (MITL). For the experimental campaign simulated in this paper, the center conductor was terminated with a hemispherical cathode, and an axial gap of 18 cm separated this cathode from a planar anode designed as a large-area bremsstrahlung converter. For an additional set of shots, a 21-cm axial anode-cathode (AK) gap was used. Inductive current monitors (B-dot probes) were used to measure the current pulse produced by the generator, with measurements taken at various axial locations along the MITL. Probes in the 8.42 cm radius center conductor measured the bound current flowing in the center conductor, while probes in the 19.85 cm radius outer

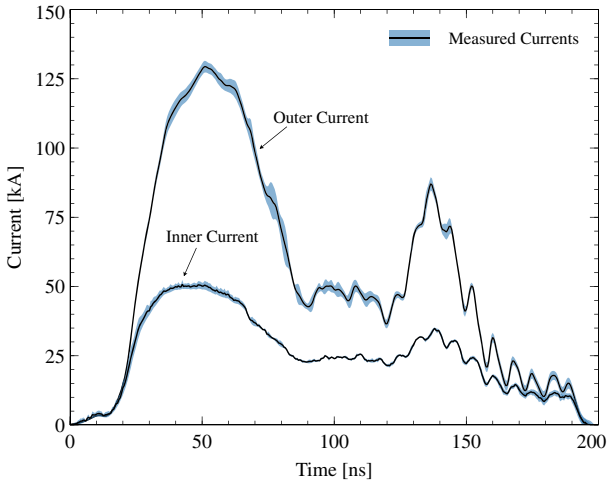

FIG. 2. Measured inner and outer currents from Mercury shot 2049, as measured 63 cm upstream of the anode. The solid lines are the mean values of the azimuthal current measurements, while the blue shaded regions show the uncertainty bound given by $\pm U_m$.

conductor measured the total current in the pulse. The difference between the inner and outer current measurements is due to current being carried by magnetically-insulated electrons flowing in the vacuum gap between the inner and outer conductors. At each axial probe location, several B-dot probes are arranged azimuthally in order to measure the azimuthal symmetry of the current in the pulse. The mean value of the azimuthal probes is used to estimate the current in the pulse at a given axial location, while the standard deviation σ of the azimuthal probe data gives an estimate of the azimuthal variation of the pulse. The uncertainty in the mean value is given by $U_m = \sigma/\sqrt{n}$, where n is the number of azimuthal probes.

In order to simulate the x-ray beam produced during this experimental campaign as closely as possible, this work will focus on the current measurements obtained in the MITL as close to the diode as possible. The B-dot probes closest to the diode are 63 cm axially upstream of the anode, and are referred to experimentally as the "load currents." The inner and outer currents measured at this location from shot 2049 (a typical shot from this series) are shown in Fig. 2 as the solid lines, and the shaded regions around the mean current show the measured current $\pm$ the uncertainty U_m in the measured current. There are four inner and four outer B-dot probes at this location, but only three of the inner probes were functioning correctly during this experiment.

III. PARTICLE-IN-CELL SIMULATIONS OF THE MERCURY MITL AND LARGE-AREA BREMSSTRAHLUNG DIODE

The measured "load currents" from shot 2049 were used to drive a particle-in-cell (PIC) simulation of the Mercury

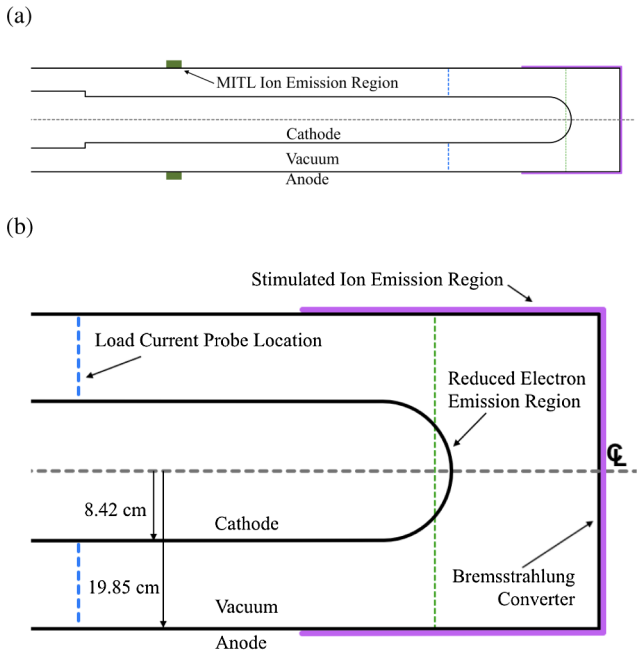

FIG. 3. (a) Geometry of the MITL PIC simulations. The green regions on the outer conductor upstream in the MITL indicate the 5 cm long region of ion emission. The outer anode radius is 19.85 cm, the inner cathode radius is 8.42 cm, and the inner radius in the upstream transition region is 10.46 cm. (b) Diagram of the diode region of the MITL simulation. The axial distance between the cathode hemisphere and the anode endplate is 18 cm. The following are shown in both (a) and (b). The last two axial centimeters of the center conductor define the region of reduced electron emission, and is indicated by the dashed green line. The region of stimulated anode ion emission is shown in magenta on the outer conductor. The axial location of the current probes (63 cm back from the anode endplate) is shown by the blue dashed line.

MITL and the large-area bremsstrahlung diode that were used in this experimental campaign. The code LSP [11] was used to perform this simulation in 2D with azimuthal symmetry. The geometry used in these simulations is shown in Fig. 3. The power pulse is driven on the left boundary of the simulation. In the simulation, the center conductor (cathode) has a step-down in radius (from 10.46 cm to 8.42 cm) just before the axial location where the electron emission from the cathode starts, similar to the step used in previous simulation work [2,12]. A space-charge limited (SCL) electron emission model was applied from the location of this step-down along the rest of the axial length of the cathode. This radial step is not present in the experiment, and is used in the simulations for two main reasons. First, the step is meant to reduce the enhanced emission that occurs at the boundary between emitting and non-emitting regions. Since this emission boundary is artificial, a current enhancement at this location would be unphysical. The step in the cathode radius reduces the local electric field and thus the emission at this location,

similar to how cathode shaping can help to smooth the emission profile in diodes [[13], and references therein]. The second reason for using a radial step on the cathode is an attempt to match the vacuum impedance of the region upstream of the step (38.4 Ω) with the operating impedance of the MITL (31.5–38.6 Ω, see Table III). This is done to reduce the possibility of a bad impedance transition, such as the ones studied in Ref. [14]. Using this step does have some possible side effects, however. Most relevant for this work is that since the step affects the structure of the electron flow layer in the MITL, it also affects the operating impedance of the MITL. This changes the balance between flow current and current bound in the cathode, and thus, for a given total current, the voltage of the pulse. More work needs to be done to examine the physical accuracy of simulations which use a cathode step, but this research is outside the scope of this paper. Figure 3(b) shows the location of the current probes 63 cm upstream of the anode end-plate (blue dashed lines), as well as various emission regions that will be described in Sec. VI.

Since the drive pulse in LSP is specified by a voltage waveform and not a current waveform, some care was needed in order to match the simulated outer current to the measured outer current. Appendix describes the method used for driving the simulation, and Fig. 4 shows the simulated inner and outer currents compared with the measured currents. The simulated outer current nearly overlays the measured outer current, showing that the method used for driving the simulation worked as designed. However, there is some difference between the measured and simulated inner currents. This will be discussed further in Sec. VI in the context of varying the emission models in the simulations. Two additional simulations were performed, where the simulated drive in the first was constructed so that the simulated current would match the measured outer current plus the uncertainty U_m, whereas the drive in the second simulation was set up so the simulated current would match the measured outer current minus the uncertainty U_m. The inner and outer currents from these simulations are used to construct the shaded uncertainty bounds on the simulated currents in Fig. 4. These two simulations give an estimate of the uncertainty in the simulation results that is due to the uncertainty in the drive pulse. Note that this does not capture the effects of the real azimuthal variations that are recorded by the B-dot probes, since the simulation is strictly two dimensional. This set of three simulations is called "Case 0" in this paper.

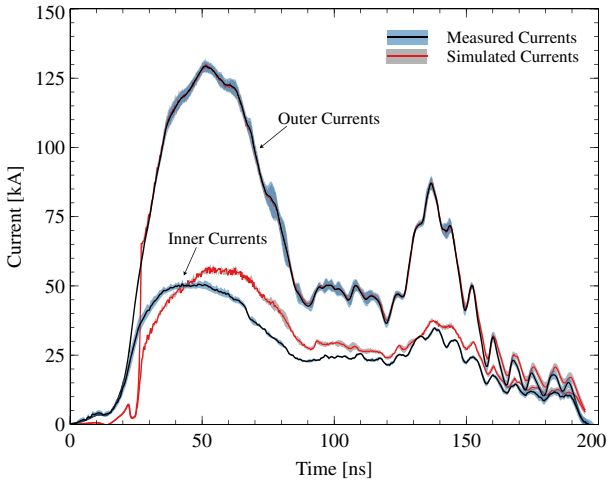

FIG. 4. Comparison of measured and simulated currents. The shaded uncertainty bounds on the "Case 0" simulation are formed using a pair of additional simulations, which are driven to match the mean outer current ± the uncertainty in the mean U_m. Note that the measured and simulated outer currents are nearly indistinguishable for most of the pulse, which shows that the drive pulse used in the simulation was working as intended.

There is one additional difference between the measured and simulated currents shown in Fig. 4, which is that the simulated currents are significantly lower than the measured currents during the first 25 ns of the simulation. This is caused by the method used to drive the simulations. Specifically, the voltage pulse is derived from the measured currents assuming a fixed MITL operating impedance. However, the impedance of the MITL is significantly different before the electron emission starts than it is afterwards. Before the cathode reaches the field threshold for electron emission, the MITL operates at the vacuum impedance for a coaxial transmission line, which is about 51.5 Ω. After the emission starts, the MITL transitions to a lower operating impedance level, which for these simulations is in the range of 31–38 Ω. Since this lower value of impedance is used to derive a voltage drive pulse, the voltage (and thus current) will be too low during the rise of the pulse. Once electron emission starts and the line transitions to its lower operating impedance, the current rises to the desired value, and matches the measured current. Adjustments to the voltage drive and emission model parameters used in the simulations may be able to decrease this discrepancy somewhat, but are beyond the scope of the present work.

IV. EXPERIMENTAL MEASUREMENTS OF THE X-RAY DOSE DISTRIBUTION

The main experimental diagnostic of the x-ray beam that was fielded during this experimental campaign was an array of TLDs. These dosimeters are composed of CaF_2 (1 mm × 1 mm cross section and 6 mm length) enclosed in a cylindrical aluminum equilibrator with walls 4 mm thick. After each shot, the TLDs are read, which gives a time-integrated measurement of the dose at the fielded location.

During this experimental campaign, TLDs were fielded in two main locations, one in the x-ray near field to measure the radial distribution of the radiation as it exits the machine, and one in the far field to measure the angular distribution of the beam. Table I shows the locations of the

TABLE I. Locations of the near-field TLDs in this experimental campaign.

TLD position number				Radial location [cm]	Angular location [deg]			
F1[a]		F2[a]		0.0	0		0	
F3[a]	F4	F5	F6	3.0	0	90	180	270
F7[a]	F8	F9	F10	6.0	0	90	180	270
F11[a]	F12[a]	F13[a]	F14[a]	9.0	0	90	180	270
F15[a]	F16	F17	F18	10.5	0	90	180	270
F19[a]	F20[a]	F21[a]	F22[a]	12.0	0	90	180	270
F23[a]	F24	F25	F26	13.5	0	90	180	270
F27[a]	F28	F29	F30	15.0	0	90	180	270
F31[a]	F32	F33	F34	18.0[b]	0	90	180	270

[a]Indicates subset of TLDs fielded on standard-resolution shots.
[b]These TLDs were not fielded when steel collimator was in place.

near-field TLDs that were mounted on the faceplate of the machine, and Table II show the locations of the far-field TLDs. Shots with the collimator in place did not have TLDs at the outermost (18 cm radius) location.

The TLD data from all of the shots with the 18-cm AK gap configuration [15] were averaged, and the results are shown as the black circles with error bars in Fig. 5. The data from the faceplate TLDs at the different angular locations listed in Table I were averaged together, which is valid if the beam was centered on-axis. The error bars on the data points in Figs. 5(a) and 5(b) show the standard deviation σ of these azimuthally averaged TLD measurements.

Due to space constraints, the far-field TLD array was only fielded on a subset of shots, shot numbers 2038–2046, seven of which used the standard-resolution angular array, and two of which used the high-resolution angular array. The mean values of the far-field TLD data are shown in Fig. 5(b), along with the standard deviation of the measurements.

TABLE II. Locations of the far-field TLDs in this experimental campaign.

TLD position number	Distance to source [cm]	Angle from axis [deg]
Z1[a]	100	0
Z2	150	0
Z3[a]	200	0
Z4	250	0
Z5[a]	300	0
A1	300	+45
A2	300	+30
A3	300	+25
A4[a]	300	+20
A5	300	+15
A6	300	+10
A7	300	+5
A8[a]	300	−5
A9[a]	300	−10
A10	300	−15
A11[a]	300	−20
A12	300	−25
A13[a]	300	−30
A14	300	−45

[a]Indicates subset of TLDs fielded on standard-resolution shots.

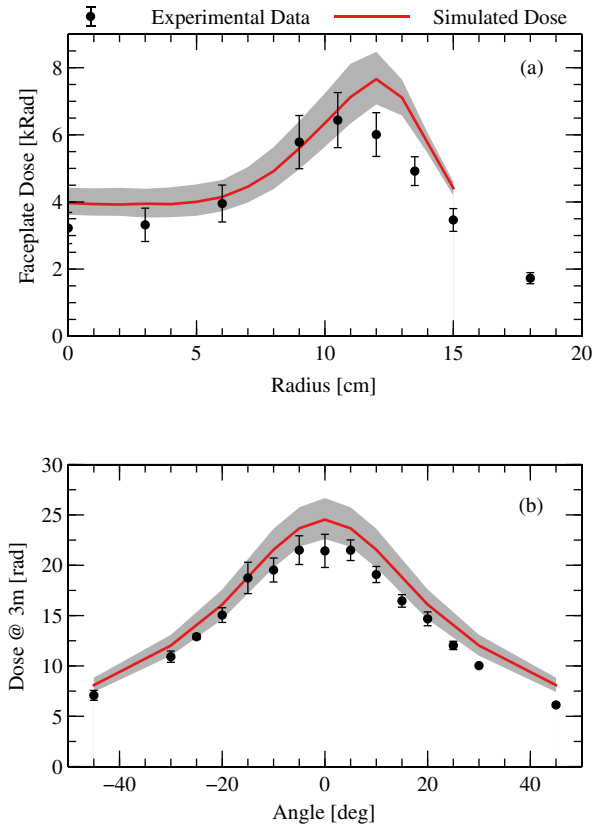

FIG. 5. Comparison of measured (black) and simulated (red) dose from the Case 0 simulations, in (a) the near field and (b) the far field. The mean of the experimental data is shown as circles, and the standard deviation is shown by the error bars. The gray uncertainty bounds on the simulated dose are computed from the simulations driven by the measured outer current ± the uncertainty in the mean.

V. MONTE CARLO SIMULATIONS OF THE BREMSSTRAHLUNG CONVERTER AND RADIATION TRANSPORT SIMULATIONS OF THE X-RAY BEAM

The production of x-rays by this large-area diode was computed using MCNP6, a well-benchmarked Monte-Carlo tool for computing radiation production and transport in experiments such as this [16,17]. Using MCNP6 allows for the accurate modeling of the converter in full three-dimensional geometry, the use of variance-reduction methods for more accurate dose calculations, and also gives a flexible starting point for any future radiation or neutron production calculations that need to be run for the analysis of this experiment. The "Monte Carlo Particle Lists" (MCPL) [18] format and associated library were used to convert electrons from the LSP simulations into a format readable by MCNP6.

The bremsstrahlung converter was modeled in MCNP6 using a simplified geometry. The converter was modeled using three discs of 20 cm radius: the first was a 787 μm thick aluminum layer used for ion suppression in the experiment, the second was a 400 μm thick tantalum bremsstrahlung converter layer, and the third was a 1.9 cm thick aluminum beam stop. The electrons are read into MCNP6 from the file generated from the PIC simulation, and they produce bremsstrahlung photons as they scatter in the converter. The properties of the resulting x-ray beam are then diagnosed by computing the dose produced in CaF_2 at the locations of the TLDs fielded in the experiment. The faceplate dose is computed at an axial distance of 0.75 cm from the downstream face of the beam stop, between 0 and 15 cm in radius. The far-field angular distribution of the beam was computed at a distance of 300 cm from the face of the beam stop, at angles of 0°, 5°, 10°, 20°, 30°, and 45° from the axis.

Note that while the PIC simulations produce time-dependent information about the electron beam, the temporal information was not retained for the MC simulations. Rather, the time-integrated electron beam was used as the source, and the MC calculation produced the time-integrated x-ray dose, which is the quantity needed for comparison with the data from the TLDs.

A. 18-cm AK gap case

Dose results for the Case 0 simulation are shown in Fig. 5. The red curves show the near-field radial distribution [Fig. 5(a)] and far-field angular distribution [Fig. 5(b)]. The gray uncertainty bounds are formed from the doses produced by the simulations driven to match the measured current $\pm$ the uncertainty U_m in the measured current. As seen in Fig. 5, the simulated and measured dose distributions agree to within the uncertainties over a large range of the far-field angular distribution, and also for about half of the near-field radial distribution.

B. 21-cm AK gap case

In order to test the effect that the axial AK gap has on the dose, an additional set of simulations was performed with a 21-cm AK gap. These simulations were driven by the current measurements from shot 2036, which was fielded with a 21-cm gap. As for the 18-cm case, a set of three simulations was performed, driven by the measured current, and the mean measured current $\pm$ the uncertainty in the mean. The results from these simulations are shown in Fig. 6 in the blue curves, along with the results from the 18-cm gap case (red curves). The measured doses are also shown in Fig. 6, with the 18-cm case shown in red circles, and the 21-cm case shown in blue diamonds. The two main differences between the 18 and 21-cm cases are: the faceplate dose peaks at a larger radius [Fig. 6(a)] for the 21-cm case and the far field dose is slightly more peaked on axis [Fig. 6(b)] for the 21-cm case. These differences are seen both in the experimental measurements and the simulation results. These observations of how the dose distributions change with AK gap spacing are consistent with results seen in previous work [2].

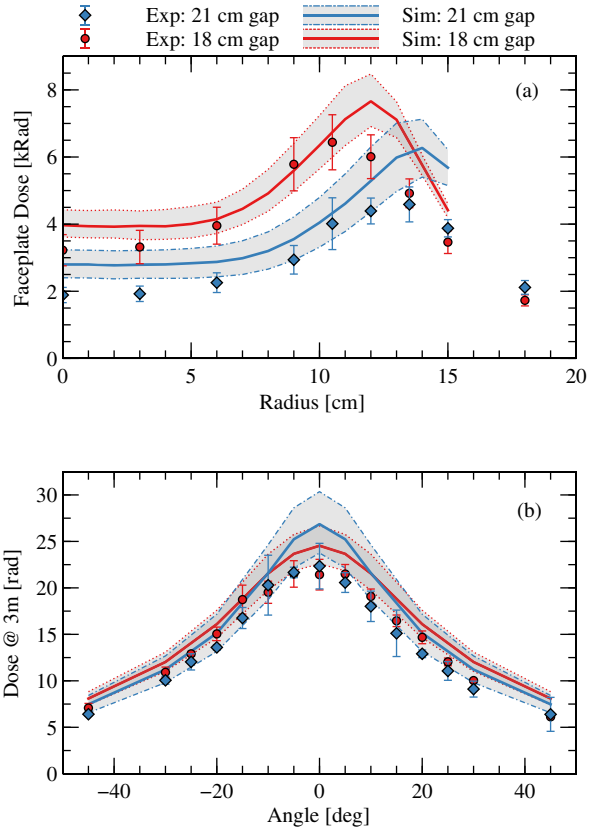

FIG. 6. Comparison of measured (points) and simulated (curves) doses from Case 0 simulations with both 18-cm and 21-cm AK gaps, in (a) the near field and (b) the far field. The faceplate dose in the 21-cm case peaks at larger radius, and the far field dose is more forward directed, both in experiment and simulation.

TABLE III. Summary of PIC simulations performed, and the various emission model parameters that were used. Blank entries in the table imply Case 0 parameter values.

	T_e [keV]	Ion model	Hemisphere emission	Operating impedance [Ω]
Case 0 ($\pm U_m$)	0.1 eV	No MITL or stimulated ions	Standard	38.6
Case M1	1			38.0
Case M2	10			36.5
Case M3	100			31.5
Case M4		MITL		37.0
Case D1		0.1% stimulated ions		
Case D2		0.2% stimulated ions		
Case D3			Reduced	
Case D4			Enhanced	

VI. PIC SIMULATIONS WITH VARIATIONS IN PHYSICS MODEL PARAMETERS

There are a variety of particle emission models that can be used in PIC simulations of the MITL and large-area diode being examined in this paper. The main emission model is space-charge limited (SCL) electron emission from the MITL center conductor and cathode hemisphere in the diode. This emission is fundamental to the operation of the MITL, and is the source of the electron beam which produces the x-rays in the bremsstrahlung converter. In addition to the electron emission model, there are two main types of ion emission that can be included in the simulations: SCL ion emission with either an electric field or thermal turn-on threshold, and stimulated ion emission in which electrons impinging on the anode release a proportional quantity of ions.

In order to examine the effect that these emission models have on the predictions of experimental dose, a series of simulations were performed using various combinations of parameters for these emission models. In this work, the emission models that were varied fall into two main categories. The first category is those models that directly affect the MITL (and only affect the diode through the effect they have on the drive pulse), and the second category is those models which directly affect the diode. The PIC simulations performed in this work, along with the various model parameters used in each, are summarized in Table III.

There were four model parameters that were adjusted in this set of simulations, two related to the MITL and two related to the diode. The MITL emission models are the thermal spread (and thus emittance) of the electrons emitted from the cathode [Cases M1–M3], and emission of ions in the MITL upstream of the "load" current monitors [Case M4]. The diode emission models are the stimulation fraction for stimulated ion production in the diode [Cases D1–D2], and reduction/enhancement of electron emission from the cathode hemisphere [Cases D3–D4].

In all of these simulations, the methods described in Appendix along with the impedances listed in Table III were used so the simulated outer current matched the measured outer current.

A. Emission models affecting the MITL

There were two emission models affecting the MITL that were examined in this work. The first is the amount of thermal spread on the electrons as they are emitted from the center conductor, and the second is allowing a small region of the outer conductor to turn on to SCL ion emission. It was found that the main effect of both of these models was to change the properties of the electron flow layer. In particular, both models acted to reduce the operating impedance of the MITL, with the resulting impedance for each simulation case listed in Table III. This in turn affects the power that can be transmitted to the diode, which is reflected in the total dose recorded in the TLDs.

The parameters chosen for both of these emission models were based partly on values that seem reasonable for the experiment, but are primarily used to show the range of simulation results that are be possible as the parameter values are varied. For example, emission of cold (0.1 eV) electrons is fairly standard for pulsed power simulations. And the maximum temperature (1 keV) was selected to obtain an azimuthal spread in electron energy that corresponds to a field strength (1 kV) that is a small fraction of the peak voltage (5 MV) in the pulse. Similarly, the upstream emission of ions from the anode in the MITL is also experimentally motivated, but not necessarily designed to correspond to any particular measurements of ion emission. Rather than try and realistically model the emission of ions from, say, a flange or vacuum port, the model used here is meant to simply show what may be possible if there is some small region of ion emission.

1. Electron thermal spread

The SCL electron emission model used in these simulations creates electrons just off the surface of the cathode. The amount of electrons produced in this model is set by the amount of charge necessary to cancel out

the perpendicular electric field at the cathode surface. These electrons are typically created cold, i.e., with zero momentum. However, an additional random momentum can be given to the electrons when they are created by sampling from a thermal velocity distribution. This distribution is described by a temperature parameter T_e. While the simulation is two-dimensional in space, the electrons are allowed to have nonzero velocity in the third, azimuthal, direction. Applying a thermal spread to the electrons when they are emitted is one of the simplest ways to create an electron beam with a spread in angular momentum in this 2D simulation, and so this model is used here to explore possible effects related to beam angular momentum. Note that we are not implying that the beam is heated to, e.g., keV temperatures by some process; rather these simulations are meant to give some insights into possible effects that could be caused by angular momentum in the beam. In the actual experiment, any beam angular momentum is more likely to be caused by azimuthal asymmetries, and any associated azimuthal component to the electric field that arises from these asymmetries.

The thermal spread resulting from using this model has several effects on the electron beam, which could contribute to differences in the x-ray beam that it produces. For example, the thermal spread gives the electrons angular momentum, which would otherwise be zero in this 2D simulation. Since this simulation is azimuthally symmetric, any angular momentum given to the electrons initially will be conserved throughout the simulation. This can act to prevent the beam from pinching on-axis. Another effect that this thermal spread can have is to increase the emittance (phase-space area) of the beam. This could potentially cause the beam to spread out radially. However, the main effect that was observed in the simulations was the change in the effective MITL impedance. The reduction of line impedance decreased the resulting dose, because for the same outer current, the voltage in the pulse is reduced.

The Case 0 simulation used $T_e = 0.1$ eV. Results from three additional simulations with varying T_e are shown in Fig. 7. These additional simulations have emission temperatures of $T_e = 1$ keV, 10 keV, and 100 keV. While these values are large when considered as temperatures, they are still small compared to the ~5 MV acceleration voltage of the machine. Note that the simulations with higher emission temperatures have significantly reduced dose, which is consistent with the reduction in line impedance for increased emission temperature (see Table III).

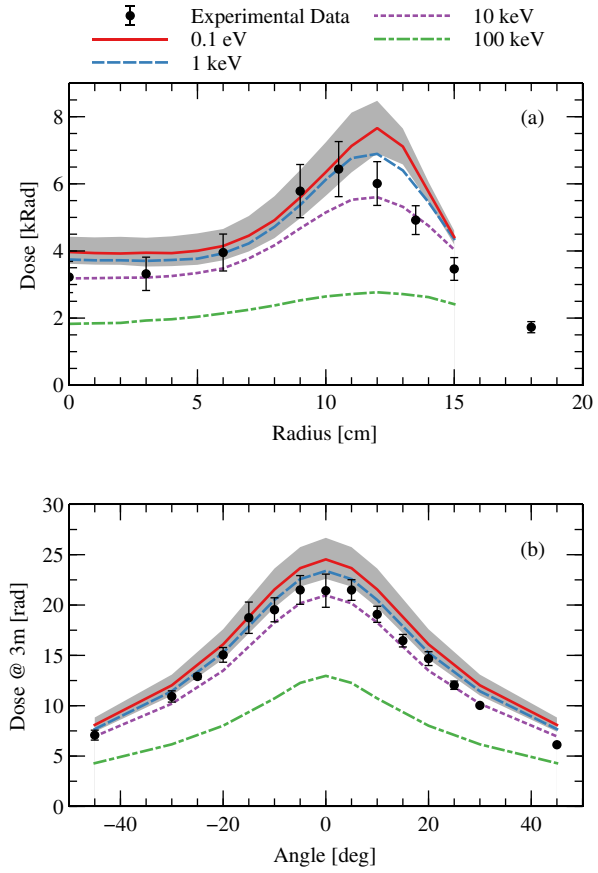

FIG. 7. Comparison of measured (points) and simulated (curves) doses from simulation Case 0 and Cases M1–M3, in (a) the near field and (b) the far field. The main effect of increasing electron emission temperature on the computed dose distributions is a reduction in total dose produced, due to its effect on the MITL operating impedance.

2. Ion emission in the MITL

The second emission model affecting the MITL that is considered in this work is the addition of ion emission from the outer conductor upstream in the MITL. The use of this model was motivated by the fact that the Case 0 simulation had too much inner current during most of the pulse (see Fig. 4). This is a sign that the MITL impedance could be different from the actual line impedance in the experiment. In order to increase the amount of flow current at a given voltage, ion emission from the anode (the outer conductor) was added in a small axial region far upstream of the current probe location. The green regions on the outer conductor in Fig. 3(a) show where the MITL ion emission is located, between 161 cm and 166 cm upstream of the anode. When the ions are emitted, they partially neutralize the electron space charge in a local region of the MITL. This causes the electron flow to lift off the cathode, and more vacuum electron flow current to be emitted. Downstream of the ion emission location, the MITL flow has settled into a new equilibrium, with more flow current and less bound current than before. This difference in inner currents can be seen in Fig. 8, where the bound cathode currents from the Case 0 simulation (without MITL ions) and the Case M4 simulation (with MITL ions) are compared. In both simulations the outer currents match the measured outer current by design. It takes a little time for the ions to emit and then affect the flow, but after about

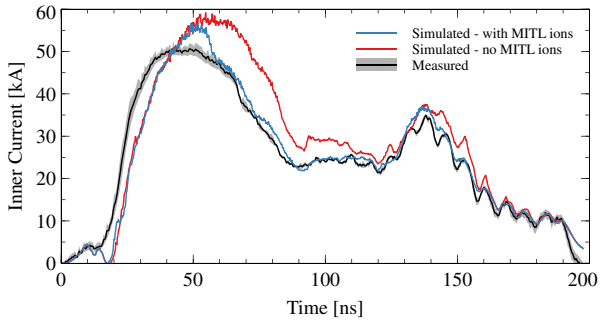

FIG. 8. Comparison of inner currents with and without MITL ions.

$t = 55$ ns, the inner current from the Case M4 simulation matches the measured current much more closely.

While the simulation with MITL ions has less cathode current than the simulation without the ions, both simulations have nearly identical anode (and thus total) currents because of the way the simulations were driven. MITL theory therefore predicts that the simulation with ions will have lower voltage [19]. Figure 9 shows the voltage from both simulations, as well as the voltage inferred from the currents in each simulation based on the rescaled Mendel formula [20]. As seen in the figure, the Mendel formula does a good job of predicting the voltage, and the drop in cathode current directly relates to a drop in voltage just after the time of the pulse peak. This can be thought of as a drop in the MITL impedance due to the ions in the simulation (Table III). This small drop in voltage leads to a 10%–15% drop in dose, as can be seen in Fig. 10.

B. Emission models affecting the diode

There were two emission models in the diode that were examined in this work. The first was the emission of stimulated ions from the anode surface, and the second was the emission of electrons from the cathode hemisphere. Figure 3 shows the region of stimulated ion emission (magenta region on the outer conductor), and the region of reduced hemisphere cathode emission 2 cm axially upstream of the end of the center conductor (green dashed line). These two models primarily affect the distribution of electrons hitting the anode surface, changing both the radial distribution of the electron beam and the average angle at which the electrons hit the anode. These effects are reflected in the radial dose distribution on the faceplate TLDs (which reflects the radial distribution of electrons), and the angular dose distribution on the far field TLDs (which reflects the distribution of the angle of incidence of the electrons).

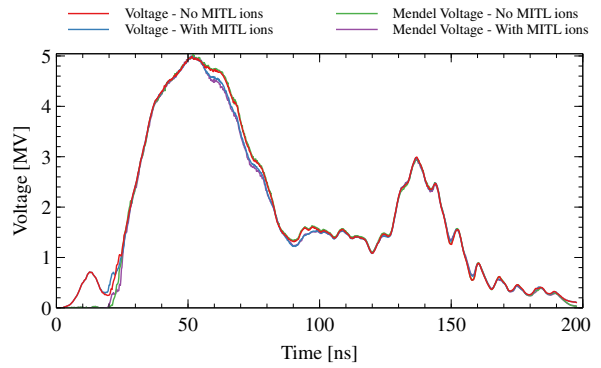

FIG. 9. Comparison of voltages from Case 0 and Case M4. The reduction in MITL line impedance due to upstream ion emission from the anode can be seen in the reduced voltage just after the pulse peak.

1. Stimulated ions

In previous work on large-area bremsstrahlung diodes at higher power [2], activation measurements were taken which were consistent with the emission of ions from the anode. It was also found that this anode ion emission was an important effect to include in the modeling. In particular, the ion emission model used was the "stimulated emission" model, where for every q coulombs of electron

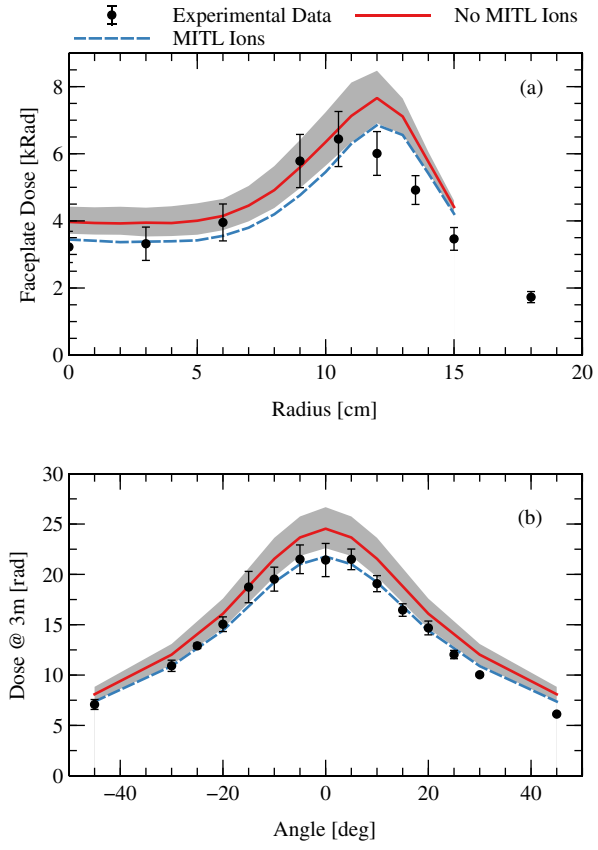

FIG. 10. Comparison of measured (points) and simulated (curves) doses from simulation Case 0 and Case M4, in (a) the near field and (b) the far field. The main effect of adding upstream ion emission in the MITL is a reduction in the dose by 10%–15%. The shapes of (a) the faceplate dose distribution and (b) the far-field dose distribution are mostly unchanged.

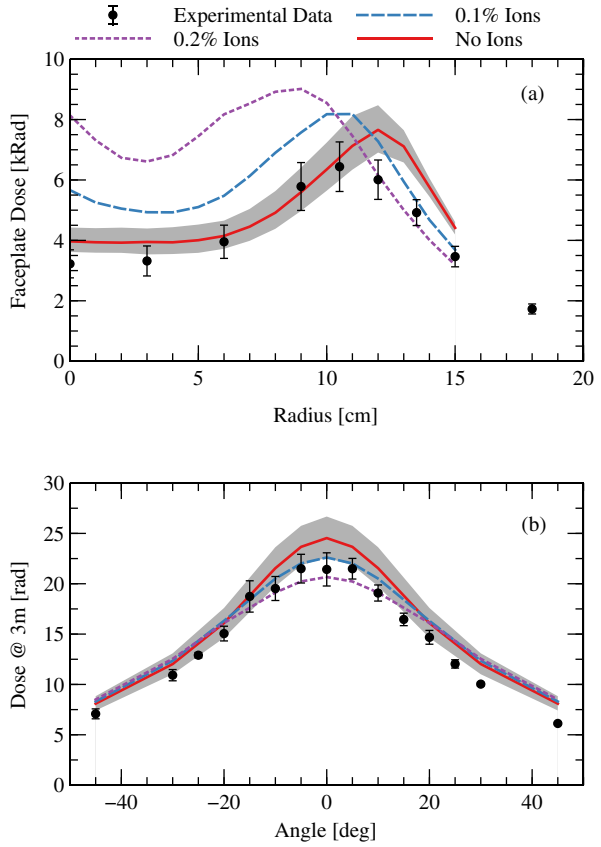

FIG. 11. Comparison of measured (points) and simulated (curves) doses from simulation Case 0 and Cases D1–D2, in (a) the near field and (b) the far field. The effects of stimulated ion emission on the computed doses are: (a) the radial location of the peak dose moves inward with increasing ion emission, and an on-axis peak in dose starts to form, and (b) the far-field dose distribution is suppressed on axis with increasing ion emission.

charge that hits the anode $f \times q$ coulombs of ion charge are emitted. The emission fraction f was found to be on the order of a fraction of a percent, with $f = 2 \times 10^{-3}$ or 0.2% giving the best fit to the data for the higher power diode examined in the previous work. In order to see if stimulated emission of ions from the anode is important for modeling the current set of experiments, two simulations were performed with stimulated ion emission, one with $f = 0.1\%$ and the second $f = 0.2\%$.

The dose results from these simulations are shown in Fig. 11. The results are consistent with previous experience working with high-power diodes. In particular, the charge carried by the ions into the diode acts to neutralize the electric self-field of the electron beam. This allows the magnetic pressure to bend the electron trajectories closer towards the axis, bringing the radial location of the beam inward. It also causes the electrons to hit the anode with a larger average angle, causing the far-field dose distribution to broaden. Both of these effects are clearly seen in Fig. 11, and both effects are larger with increasing emission fraction.

Note that these simulation results seem to lead to a different conclusion than the previous work. Here, the case with no ions seems to fit best, and the simulation results seem to suggest that $f = 0.05\%$ may be the largest value to use in order to match the experiment, rather than the 0.02% obtained previously. However, to reiterate, these simulations were not performed in order to try and obtain the best match to the data. Rather they are done to show the sensitivity of the results to the values of the model parameters. Care should therefore be taken when attempting to draw conclusions about what value of f gives the best match to experimental measurements.

2. Suppressed/enhanced electron emission from the hemisphere

The two main discrepancies between the simulated and measured faceplate dose are the radius of the annular peak of the dose, and the magnitude of the on-axis dose. In order to examine possible simulation models which might address the second issue, two additional simulations were

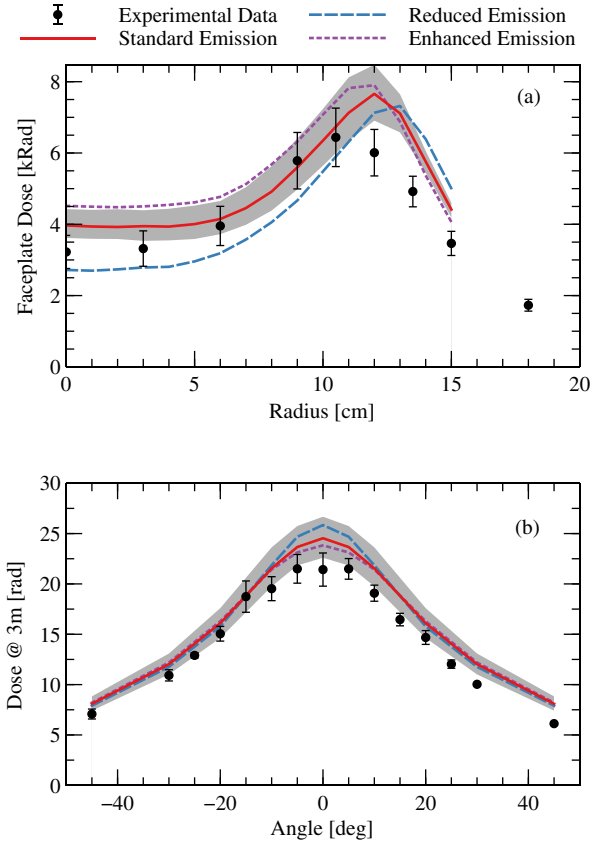

FIG. 12. Comparison of measured (points) and simulated (curves) doses from simulation Case 0 and Cases D3–D4, in (a) the near field and (b) the far field. Changes in electron emission from the cathode hemisphere causes: (a) changes in the on-axis faceplate dose and peak radius of annular beam, and (b) slight changes to the peak shape of the angular distribution of the far-field dose.

performed where the electron emission from the cathode hemisphere was varied. In the first simulation, the emission has been reduced artificially to 0.3 times the Child-Langumiur current density. In the second, emission was artificially enhanced to 1.7 times the Child-Langumiur current density. The change in emission in both cases was applied to the last two centimeters (axially) of the center conductor, which corresponds to locations on the hemisphere with radii of less than about 5.45 cm. This region is demarcated in Fig. 3 by the dashed green line.

As seen in Fig. 12(a), reducing the emission from the hemisphere reduced the on-axis dose, while enhancing the emission increased the on-axis dose. Changing the hemisphere emission also changed the radius of the annular beam: the radius increased when emission was suppressed, and the radius decreased when emission was enhanced. This is expected since changes to the axial bias current also change the magnetic force which pulls the electron beam to smaller radius. The change in hemisphere emission also slightly affected the far-field dose distribution. The case with reduced emission had a more forward directed beam, which is seen in the far-field dose being more peaked on-axis in Fig. 12(b). Enhanced hemisphere emission caused the beam to be slightly broader in angle.

VII. CONCLUSIONS

Detailed simulations of the x-ray beam produced by a large-area bremsstrahlung diode have been completed, and the resulting dose distributions agree fairly well with dose measurements taken during a recent experimental campaign on the Mercury pulsed power accelerator. This agreement is obtained by using a set of well-benchmarked simulation tools: LSP for PIC simulations of the diode and MCNP6 for radiation production and transport. By carefully driving the simulations in such a way that the current pulse in the simulations match the measured current pulse, reasonable agreement was obtained between the measured and simulated doses, with some minor differences. There are, however, several different physics models used in these simulations which could potentially affect the results. In order to understand the range of variations in dose which could be realized by adjusting the model parameters, an additional set of simulations was performed.

Additional simulations where electron and ion emission model parameters were adjusted have demonstrated the effect that these models have on the resulting dose distributions. These results suggest ways that the simulated doses can perhaps be brought into even better agreement with the measured doses, and also provide a sense of the variations that can result from changing the model parameters. For example, adding a small amount of ion emission from the anode in the MITL was found to slightly reduce the operating impedance of the MITL. This has two main effects on the simulation results. First, it brought the simulated inner current into closer agreement with the measured inner currents, suggesting this may be a more accurate model of the behavior of the MITL in the experiment. Second, due to the voltage reduction associated with the reduced operating impedance, the simulated doses also were slightly reduced bringing them into even better agreement with the measured far-field dose [see Fig. 10(b)].

Several of the emission models that were examined were of emission within the diode itself. It was found that these models primarily affect the radial and angular distributions of the electron beam, rather than the overall radiation yield. While none of the models tested were able to fully reproduce the measured faceplate dose distribution, they do illustrate the effect that various types of electron and ion emission models have on the electron beam produced in this diode. This increased understanding of the details of the diode operation could in future work lead to higher fidelity simulations of this type of bremsstrahlung diode.

There are several places where follow-up research would be valuable. One question to address is the issue of the simulated currents being too low early in the pulse. Some preliminary simulations suggest that increasing the drive voltage during the first 20 ns or so of the pulse will bring the simulated currents into better agreement with the measurements, resulting in 3%–5% increase in the near-field dose, but only $\lesssim 1\%$ variation in the far-field dose. Understanding these effects and coming up with a more accurate and self-consistent way to drive the simulation would be interesting future research topics. Other possible topics include: the effect of 3D asymmetries (which would require fully 3D simulations), the effect of flow electrons emitted in the adder region of the IVA (which would require simulations of the full machine), and comparison of the simulated x-ray beam to additional diagnostics such as x-ray pin-hole camera images and Compton spectrometer data.

In addition to these time-integrated diagnostics, various time-dependent diagnostics could help further constrain the model parameters used for these simulations. For example, data from time-resolved x-ray photodiodes fielded at different angles can provide information about the dynamics of the x-ray beam throughout the pulse. This data could be compared to a new set of time-resolved MC simulations of the generation and transport of the x-ray beam. Since the radius and average angle of the electron beam are affected by particle emission in the diode, this would give another way to constrain the parameters used in these models.

ACKNOWLEDGMENTS

The authors wish to thank Tony Culver and Brian Sobocinski for all the effort they put into operating the Mercury generator, and especially for the work they put into fielding and reading the extensive number of TLDs used in this experimental campaign. This work was supported by the U.S. National Nuclear Security Agency and the U.S. Department of Energy. This work at Los

Alamos National Laboratory was performed under the auspices of the U.S. Department of Energy by Los Alamos National Security, LLC under Contract No. DE-AC52-06NA25396. (LA-UR-19-20335).

APPENDIX: DETAILS OF VOLTAGE DRIVE FOR LSP SIMULATIONS

In order to drive the LSP simulations of the large-area bremsstrahlung diode in a manner as closely resembling the experiment as possible, the approach was taken to adjust the applied voltage drive in such a way that the current at the "load" location (63 cm from the anode) in the simulation matched the measured "load current" as best as possible. The adjustment of the voltage pulse is necessary because LSP does not have a way to drive a specified current, only a specified voltage. Fortunately, the total current is related closely to the voltage for an MITL such as this. In particular, given a desired current pulse $I(t)$, the voltage in the simulations is found to follow this relation

$$V(t) \simeq V_1 \left(\frac{I(t)}{I_1} \right)^p, \tag{A1}$$

where for most cases $p \simeq 1.2$. The relation between the amplitudes I_1 and V_1 is set by finding an approximation to the MITL operating impedance Z_1 near the peak of the pulse: $V_1 = Z_1 I_1$. This relationship was used with the measured currents to derive a voltage pulse suitable for driving the LSP simulations. Note that the impedance in the simulation depends on some of the simulation model parameters, and thus for some cases, the simulations were first run to get an estimate of Z_1, and then this value of impedance was used to derive a new voltage pulse that would give better matching between simulated and measured currents. Note that the power $p = 1.2$ gave a good fit for almost all cases. The worst case was for the electron emission with 100 keV temperature

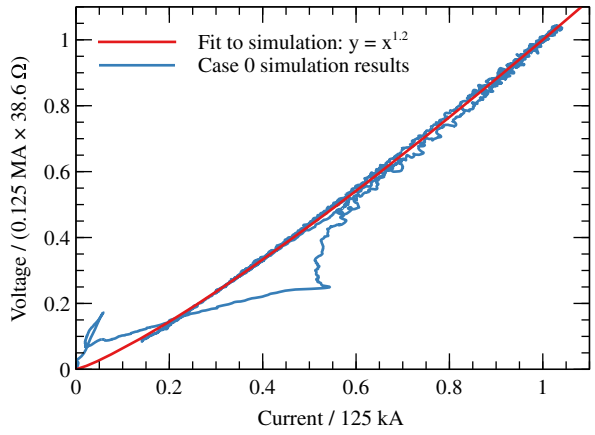

FIG. 13. Comparison between voltage and total current, for simulation Case 0. The part of the simulation pulse that lies farthest from the fit is from early in the pulse, before the flow current is established and while the voltage is still relatively low.

spread. In this case, $p = 1.25$ seemed to give slightly better agreement, especially near the start of the pulse. However, $p = 1.2$ was used for all cases for consistency. The value of Z_1 used in each simulation is listed in Table III, and the fit for Case 0 is shown in Fig. 13. Note also that Eq. (A1) is entirely empirical, and is only used in order to have a well defined and consistent way to get a shape for the simulation drive pulse that will give the desired total current in the simulation. While there are some differences between the desired and simulated outer currents (especially early in the pulse), Fig. 4 shows that using this formula gives the desired current throughout the majority of the simulated pulse.

[1] R. J. Allen, R. J. Commisso, G. Cooperstein, P. F. Ottinger, and J. W. Schumer, Extension of the operating point of the Mercury IVA from 6 to 8 MV, in *Proceedings of the 18th IEEE International Pulsed Power Conference, Chicago, IL* (Omnipress, Madison, WI, 2011), pp. 1036–1041.

[2] J. C. Zier, D. Mosher, R. J. Allen, R. J. Commisso, G. Cooperstein, D. D. Hinshelwood, S. L. Jackson, D. P. Murphy, P. F. Ottinger, A. S. Richardson, J. W. Schumer, S. B. Swanekamp, and B. V. Weber, High-power, photo-fission-inducing bremsstrahlung source for intense pulsed active detection of fissile material, Phys. Rev. ST Accel. Beams **17**, 060401 (2014).

[3] D. R. Welch, D. V. Rose, N. Bruner, R. E. Clark, B. V. Oliver, K. D. Hahn, and M. D. Johnston, Hybrid simulation of electrode plasmas in high-power diodes, Phys. Plasmas **16**, 123102 (2009).

[4] N. Bruner, D. Welch, K. Hahn, and B. Oliver, Anode plasma dynamics in the self-magnetic-pinch diode, Phys. Rev. ST Accel. Beams **14**, 024401 (2011).

[5] N. Bennett *et al.*, Shot reproducibility of the self-magnetic-pinch diode at 4.5 MV, Phys. Rev. ST Accel. Beams **17**, 050401 (2014).

[6] D. Cai, L. Liu, J.-C. Ju, T.-Y. Zhang, X.-L. Zhao, and H.-Y. Zhou, Simulative research on the anode plasma dynamics in the high-power electron beam diode, Phys. Plasmas **22**, 073108 (2015).

[7] N. Bennett, D. R. Welch, T. J. Webb, M. G. Mazarakis, M. L. Kiefer, M. D. Crain, D. W. Droemer, R. E. Gignac, M. D. Johnston, J. J. Leckbee, I. Molina, D. Nielsen, R. Obregon, T. Romero, S. Simpson, C. C. Smith, F. L. Wilkins, and D. Ziska, The impact of plasma dynamics on the self-magnetic-pinch diode impedance, Phys. Plasmas **22**, 033113 (2015).

[8] D. V. Rose, C. L. Miller, S. Portillo, and D. R. Welch, Electrode-plasma-driven radiation cutoff in long-pulse, high-power microwave devices, Phys. Plasmas **20**, 034501 (2013).

[9] I. Langmuir and K. B. Blodgett, Currents limited by space charge between coaxial cylinders, Phys. Rev. **22**, 347 (1923).

[10] D. R. Welch and T. P. Hughes, Effect of target-emitted ions on the focal spot of an intense electron beam, Laser Part. Beams **16**, 285 (1998).

[11] D. R. Welch, B. V. Oliver, D. V. Rose, R. B. Campbell, and T. A. Mehlhorn, in *Proceedings of the 11th International Conference on Emerging Nuclear Energy Systems, Albuquerque, NM*, NTIS number PB2003-102104 (U.S. Dept. of Commerce, Technology Administration, National Technical Information Service, Springfield, VA, 2002), pp. 267–274.

[12] S. B. Swanekamp, J. R. Angus, G. Cooperstein, P. F. Ottinger, A. S. Richardson, J. W. Schumer, and B. V. Weber, Particle-in-cell simulations of electron beam control using an inductive current divider, Phys. Plasmas **22**, 113108 (2015).

[13] P. Zhang, Á. Valfells, L. K. Ang, J. W. Luginsland, and Y. Y. Lau, 100 years of the physics of diodes, Appl. Phys. Rev. **4**, 011304 (2017).

[14] J. G. Leopold, R. Gad, and I. Navon, Flow dynamics along complex magnetically insulated transmission lines, IEEE Trans. Plasma Sci. **40**, 1878 (2012).

[15] The 18-cm AK gap shots with good TLD data were shots 2038-2073, 2075-2092, and 2097-2132.

[16] C. Werner *et al.*, MCNP6.2 Release Notes, Los Alamos National Laboratory Technical Report No. LA-UR-18-20808, 2018.

[17] C. Werner, MCNP Users Manual—Code Version 6.2, Los Alamos National Laboratory Technical Report No. LA-UR-17-29981, 2017.

[18] T. Kittelmann, E. Klinkby, E. Knudsen, P. Willendrup, X. Cai, and K. Kanaki, Monte Carlo Particle Lists: MCPL, Comput. Phys. Commun. **218**, 17 (2017).

[19] C. W. Mendel, D. B. Seidel, and S. E. Rosenthal, A simple theory of magnetic insulation from basic physical considerations, Laser Part. Beams **1**, 311 (1983).

[20] P. F. Ottinger and J. W. Schumer, Rescaling of equilibrium magnetically insulated flow theory based on results from particle-in-cell simulations, Phys. Plasmas **13**, 063109 (2006).